

We are IntechOpen, the world's leading publisher of Open Access books Built by scientists, for scientists

6,900

Open access books available

186,000

International authors and editors

200M

Downloads

Our authors are among the

154

Countries delivered to

TOP 1%

most cited scientists

12.2%

Contributors from top 500 universities



WEB OF SCIENCE™

Selection of our books indexed in the Book Citation Index
in Web of Science™ Core Collection (BKCI)

Interested in publishing with us?
Contact book.department@intechopen.com

Numbers displayed above are based on latest data collected.
For more information visit www.intechopen.com



High Speed Rotors on Gas Bearings: Design and Experimental Characterization

G. Belforte, F. Colombo, T. Raparelli, A. Trivella and V. Viktorov

Additional information is available at the end of the chapter

<http://dx.doi.org/10.5772/50795>

1. Introduction

Gas bearings are employed in a variety of applications from micro systems to large turbo-machinery. As they are free from contaminants if supplied with clean air, gas bearings and pneumatic guide-ways are often used in food processing, textile and pharmaceutical industries. The new research works are focused on expanding the applications of gas bearings, in particular at very high speeds. Dental drills for example operate at speeds of over 500 krpm and it seems that a limit for gas bearings without cooling is 700 krpm [1]. Nevertheless in [2] a spindle with 6 mm diameter that operated at 1.2 million rpm is described.

Because of the extremely close manufacturing tolerances that air bearings require and the lack of standard large scale production models, their costs are not at all competitive with those of the rolling bearings in common use. In order to determine whether the initial costs associated with investing in gas bearings will result in savings, each type of technology should be carefully examined. The service life of gas bearings is in fact practically unlimited, since they require almost no maintenance and do not wear.

Many investigations of air bearings have been conducted using experimental, numerical and theoretical approaches with analytical models, e.g. [3-6]. However research is still necessary to improve stiffness, load capacity and stability. At present, research studies potential designs individually to seek the main requirements for a particular application. For dynamic gas bearings, applications are currently limited to those involving low power, though an increasing amount of work is focusing on developing reliable solutions for higher-power uses. Machine tool applications, for example, require a stiffness comparable to those of the rolling bearings in common use; in very high speed applications operational stability is essential. In many cases, parameters such as the number and diameter of supply holes, their arrangement, and supply system geometry come into play. Where rotor stability under low

load at very high rotational speed is the prime consideration, designs which bring rotor orbit amplitude down to acceptable levels can be adopted.

The design of gas bearings involves matching the load and stiffness requirements with bearing clearance, orifice type, flow rate and air supply pressure. Numerical calculations can assist bearing design, but their validity must be verified through basic experimental investigations. Therefore at the Mechanical and Aerospace Engineering Department of Politecnico di Torino both experimental and numerical methods were used to design gas bearing spindles and other rotors.

This chapter provides an overview on the design of rotor-gas bearing systems and the experimental activity carried out. For each application developed it is also presented the state of the art that can be found in literature. The models developed to simulate the rotor-bearings systems are described in a separate paragraph.

Four prototypes of high speed spindles were designed using gas bearings: a completely pneumatic spindle, an electro-spindle designed for machine tools, a rotor for textile applications and a mesoscopic spindle devoted to high precision machining of micro-parts at very high speeds.

2. The pneumatic spindle

In high speed machining there are some applications for drilling, milling, and grinding, in which gas bearings are used to support the spindle [7,8]. The spindle technology in ultra-precision turning and grinding is nowadays an integration of the motor, spindle shaft and the bearings. In general these spindles have diameters smaller than 20 mm and it is difficult to find an application with a pneumatic spindle of greater diameter. In reference [9] a prototype for woodworking with spindle diameter 60 mm is described.

The prototype developed at Politecnico di Torino is capable of achieving 100000 revolutions per minute and operates at an air supply gauge pressure of 0.4-0.6 MPa. It was designed with the purpose of obtaining high load capacity and stiffness on bearings, so the spindle diameter is greater than spindles designed to achieve 200000 rpm.

The spindle is shown in Figure 1, which illustrates how the housing (4) is constrained to the base through flange (5) and journal (6). Radial support is provided by bushings (7) and (8), while axial thrust is opposed by disks (9)-(11).

The housing is made of 18 Ni Cr Mo 5 steel, while the rotor (Figure 2) (mass 7 kg, diameter 50 mm, length 459 mm) is made of 88 Mn V 8 Ku tool steel quenched and tempered to a hardness of 60 HRC. The rotor was also aged in liquid nitrogen for 5 h and dynamically balanced to a grade better than ISO quality grade G-2.5. The nose (12) to which loads are applied is secured to one end of the rotor, while the driving turbine (13) is integral with the other end. Bushings are made of the same material as the housing and have an axial length of 100 mm.

The bearings were designed to maximize the stiffness because of the importance of this parameter during cutting operations. They are provided with four circumferential sets of four 0.25 ± 0.01 mm diameter radial holes, drilled in brass inserts as shown in Figure 3.

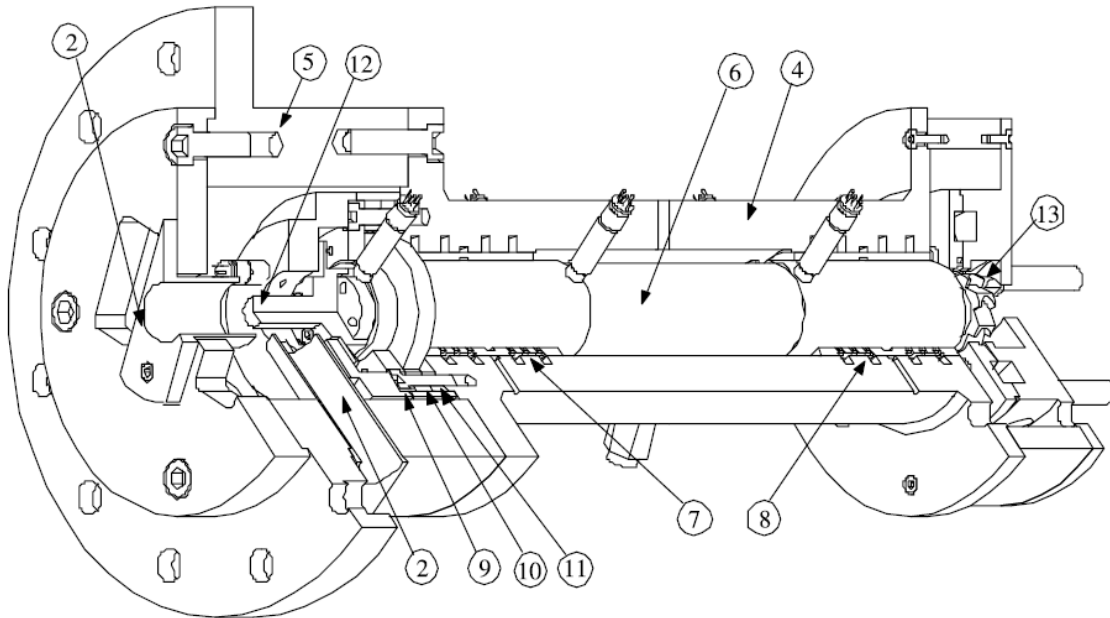


Figure 1. Section of the pneumatic spindle

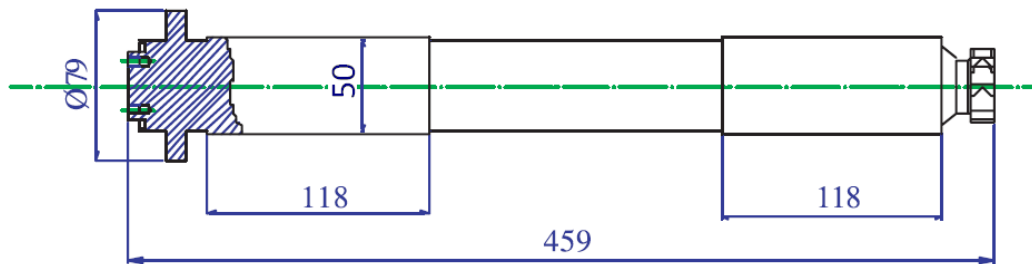


Figure 2. Rotor

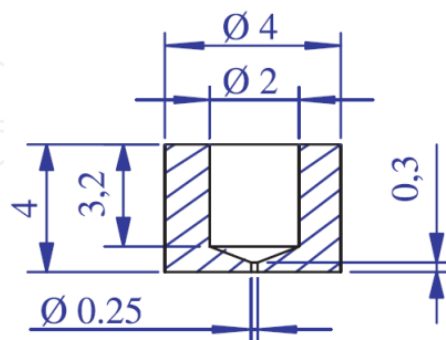


Figure 3. Brass insert with the supply hole

The axial thrust (Figure 4) is controlled by two disks (9) and (11) facing the flange on the journal. These disks are separated by a ring (10) whose thickness determines the size of the air gap. Supply air is delivered from an axial hole in the housing, is distributed through a

circumferential slot, and then crosses a series of axial and radial channels machined in the disks to reach 0.25 ± 0.01 mm diameter axial nozzles (14) and (15), which are also machined in inserts. Both the bushings and the disks were surface hardened and machined to produce a surface roughness of 0.2 and $0.4 \mu\text{m}$, respectively at the air gaps.

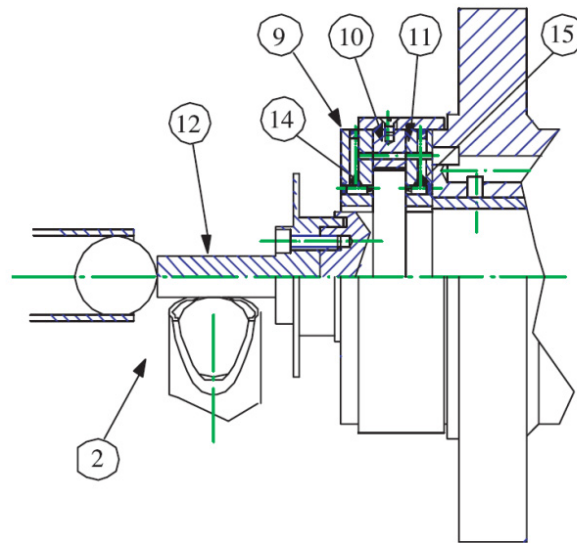


Figure 4. Enlargement of the thrust bearing and the nose

Radial and axial forces are applied to nose (12) by means of load devices (2). These devices are made of a hollow cylinder containing a calibrated sphere with a diametral clearance of $40 \mu\text{m}$. When the cylinder chamber is supplied, the sphere is pushed against the nose and at the same time supported, so that it can rotate against the nose without sliding. Radial and axial forces can thus be transmitted to the rotor even when the latter is in motion.

Supply air for the turbine (Figure 5) crosses pre-distributor (16) in the axial direction to reach annular chamber (17), from which distributor (18) leads to eight tangential channels. Air is exhausted after actuating the turbine. Open loop speed control is accomplished by establishing turbine supply pressure.

Bearing supply is separate from turbine supply. Should the air supply fail, a reservoir enables the bearings to operate during rotor deceleration, thus preventing the rotor from seizing on the bushings or disks. Supply lines are provided with two air filtration units featuring borosilicate glass microfiber cartridges whose filtration efficiency is 93 and 99.99% respectively with $0.1 \mu\text{m}$ diameter particles. For the bearing supply line, an activated carbon coalescent filter was added to eliminate any oil vapors.

The test bench uses five capacitive displacement transducers with $0.1 \mu\text{m}$ resolution, $500 \mu\text{m}$ full scale reading and 6 kHz passband. One of the transducers is used axially to measure the relative position of the rotor and thrust disks. The other four are installed radially on two different planes at right angles to the rotational axis. Rotor displacement in the bushing can thus be measured in both plane directions. The signals from these sensors are amplified by

appropriate charge preamplifiers and then conditioned in a module containing a single oscillator and a demodulator for each channel. The sensitivity of these sensors is constant within the 0-10 V linearity range.

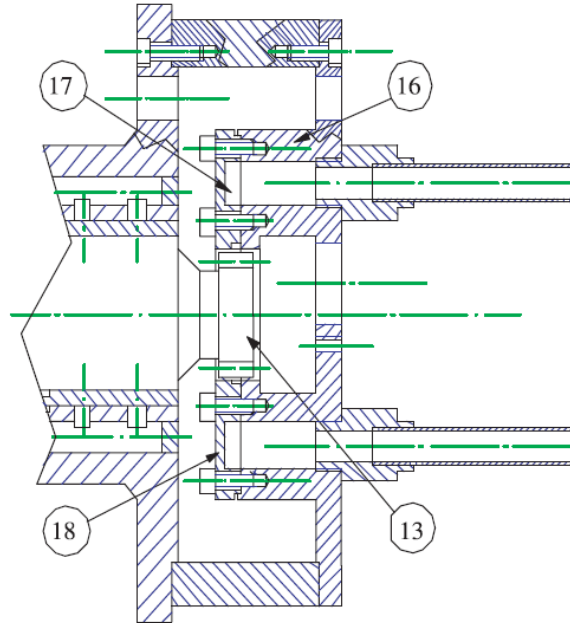


Figure 5. Enlargement of the driving turbine

To determine the journal rotational speed, an optical tachometer provided with an emitter and receiver is used, with a digital counter. Several thermocouples are also used to measure the temperature of the outer housing surface and of the air issuing from the bearing exhaust ports.

Dimensional checks were carried out to know with good precision the air gap of the bearings and the diameters of the holes. The mean inside diameter of the bushing and the mean external diameter of the rotor were measured with a precision height gage (Mitutoyo Linear Height). The mean radial air gap was calculated as the difference between the radius of the bushing and the radius of the rotor. The axial mean air gap between thrust flange and disks is calculated as the difference between measured ring and flange mean thicknesses. Results are compared with the nominal air gaps in Table 1.

	Radial air gap (μm)	Axial air gap (μm)
exp. value	26	18
nominal value	25	20

Table 1. Measured values of the air gaps

The diameters of the holes that supply the bearings were checked with an optical fiber camera with 50x and 100x magnifying lenses. Table 2 shows the measured mean diameters of the holes, with the indication of the frequency. These holes were produced using microdrills.

Diameter (mm)	Frequency
0.24	25
0.245	7
0.25	16

Table 2. Measured diameters of the supply holes

Tests were carried out to determine the bearing stiffness with the rotor stationary. The radial stiffness measured in correspondence of the nose at 120 mm from the front side of the bearing is 18 N/μm at 0.6 MPa supply gauge pressure. The axial stiffness is 27 N/μm at the same supply pressure.

Figure 6 shows the thermal transient at 40 krpm for spindle internal and external temperature measurements. The internal temperature is close to that of the air issuing from the exhaust ports. This is in accordance with the results indicated in the literature, see e.g. [10].

Rotor orbits at the two radial bushings were recorded at speeds up to 50 krpm, although tests have gone up to 80 krpm.

Figure 7 shows an example of orbits at 45 krpm, both in forward precession. Sensors 1 and 2 are for the bushing on the turbine side, while 3 and 4 are for the bushing on the motor side. These orbits, which were measured with zero radial and axial loads, are synchronous and stable. As signal frequency analysis indicated that no peak appears at a frequency of around half the rotation frequency, unstable whirling does not occur.

The centrifugal forces effect has been taken into account during the rotor designing. The radial deformation of the rotor far from its flange is visible in Figure 8.

The approaching of the external surface of the rotor to the sensors has also been considered in order to plot the orbits.

By means of a finite element code a circumferential groove was designed in proximity of the rotor flange in order to compensate the deformation due to the centrifugal force of the flange.

In Figure 9 the calculated deformation with the circular groove (depth 0.5 mm, length 10 mm) is visible. The deformation is enlarged with respect to the rotor profile. Also thermal effects on the relative distance between rotor and sensors, mounted on the housing, have been taken into account in order to individuate the centre of the orbit.

3. The electro-spindle

In literature can be found examples of air bearing electro-spindles for high speed and high precision applications, see for example references [11-13]. The electro-spindle developed at Politecnico di Torino [14], shown in Figure 10, is composed of a rotor of 7 kg mass, 50 mm diameter and 479 mm length. It is supported by air bearings and accelerated by means of an

asynchronous motor mounted on one end of the spindle. On the opposite end of the rotor a clamping tool is mounted.

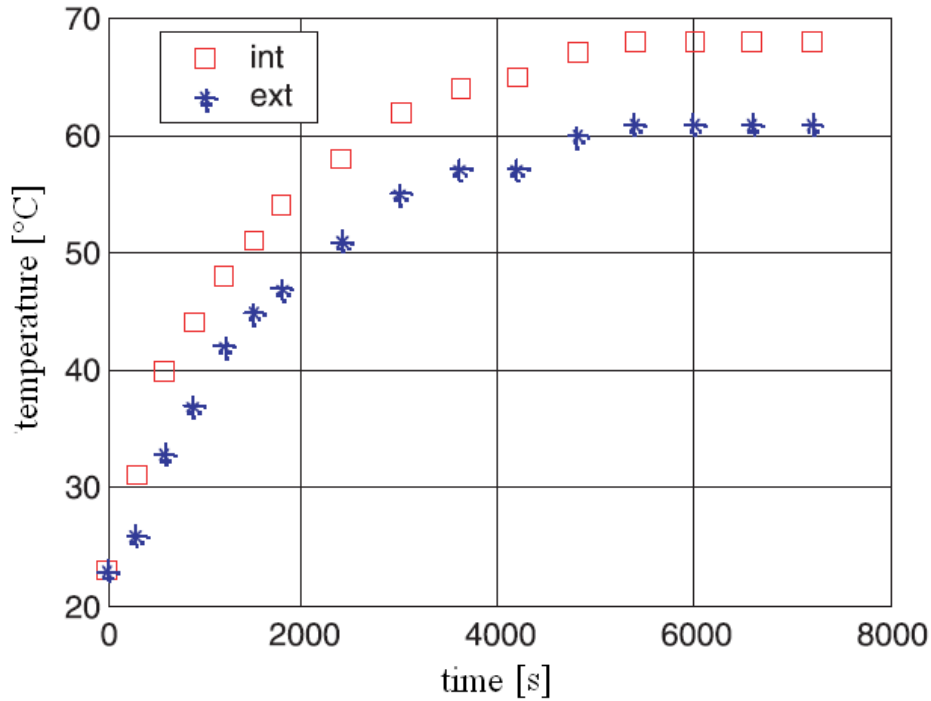


Figure 6. Thermal transient

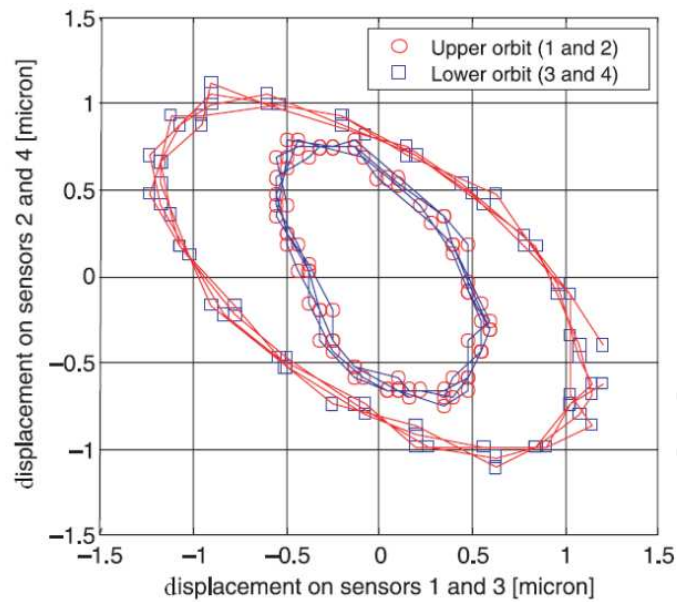


Figure 7. Rotor orbits; $\omega = 45$ krpm

Figure 11 shows a section of the electro-spindle with carter (1), rotor (2), two bushings (3) and double thrust bearing (4). Motor (5) is of the two-pole squirrel-cage type controlled by an inverter. Speed range is up to 75 krpm and power is 2.5 kW. A clamping tool designed for high-speed is screwed onto the left end of the rotor. By mounting a tool on the spindle it is possible to test the dynamic behaviour of the rotor also during the machining process.

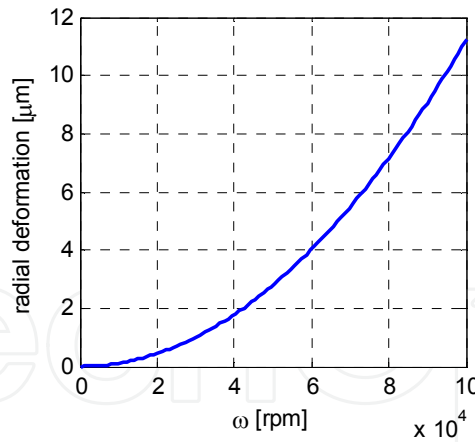


Figure 8. Centrifugal expansion of the rotor in correspondence of the bushings (diameter 50 mm)

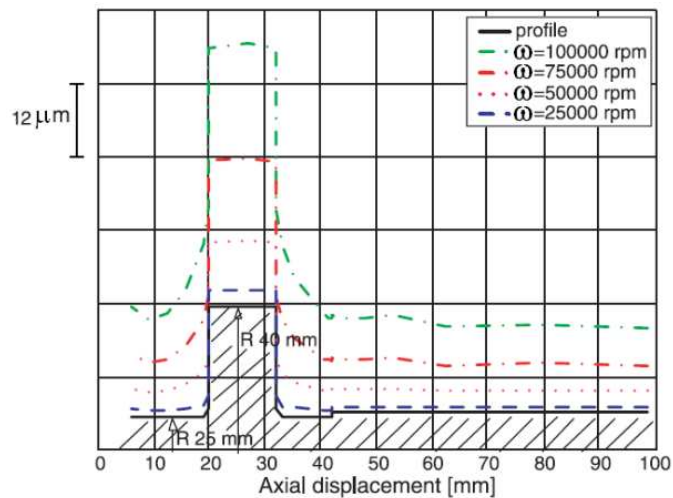


Figure 9. Rotor deformation due to centrifugal force in correspondence of the flange at different rotational speeds

The radial bearings feature cylindrical barrels. Each barrel has four sets of supply ports diameter 0.25 ± 0.01 mm arranged 90 degrees apart. The thrust bearing, similar to the one described in [15], is composed of two disks facing the flange on the journal. Each disk has 8 axial nozzles dia. 0.2 ± 0.01 mm positioned on the mean diameter.

The system is provided with a closed cooling circuit that controls the temperature of the motor and of the discharge air. Without refrigeration and with ambient temperature 298 °K, at 60000 rpm the temperature would reach 383 °K after two hours due to power losses on bearings.

An optical tachometer facing the rotor was provided to measure rotational speed. Four capacitance displacement transducers were inserted radially and at right angles in the carter facing the rotor to measure dynamic runout. Two were positioned on motor side, the other two on thrust bearing side.

Clearances were measured moving the rotor axially and radially until contact is made. It was found that axial and radial clearances are about 15 μm and 20 μm respectively.

In order to measure radial and axial stiffness of the tool, the electro-spindle is mounted on a test rig designed for the purpose with proper load devices. Radial forces were measured at different supply pressures (Figure 12) at $\omega=0$. Figure 13 shows the axial load capacity readings for 0.3, 0.5 and 0.7 MPa supply absolute pressure. The load device was used for positive displacements and weights were applied to obtain the curve with negative displacements.

The rotor orbits depicted in Figure 14 were measured at the same supply pressure. Due to the rotor centrifugal expansion these orbits appear not to be centered in the bushings because the relative rotor-sensor distance decreases. The spindle was tested up to 53000 rpm and the tests were stopped because of the high rotor vibration. The permissible residual imbalance should be diminished in order to allow tests at higher speeds. Anyway the whirl instability did not occur and the imbalance response was only synchronous.



Figure 10. Photo of the electro-spindle

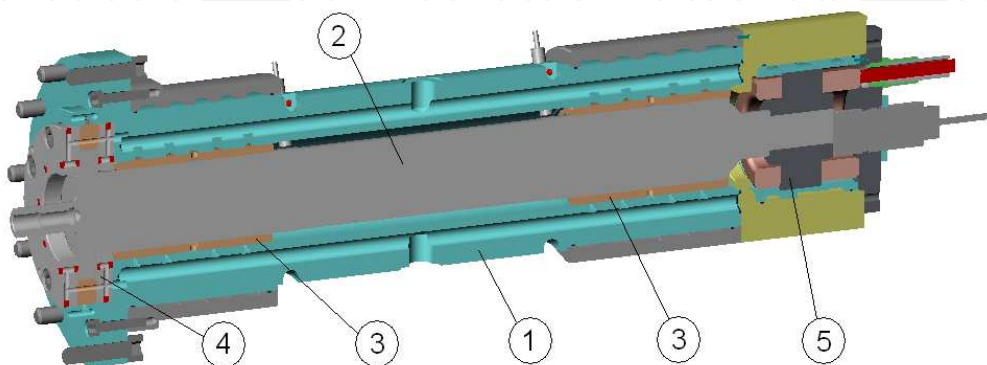


Figure 11. Schematic section of the electro-spindle

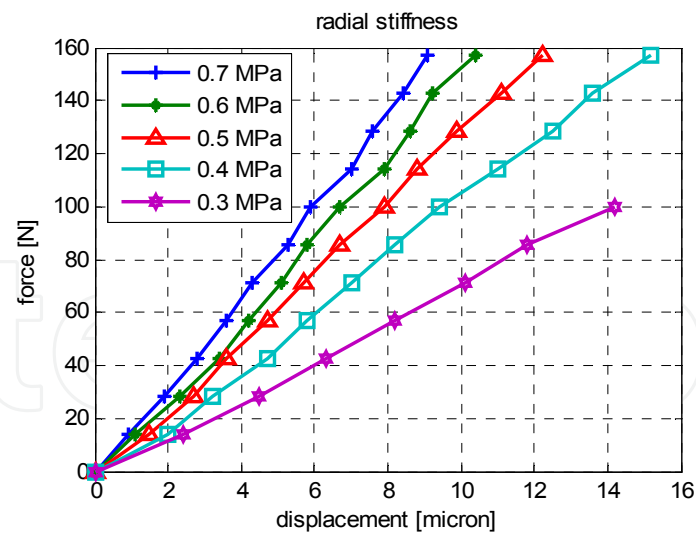


Figure 12. Radial force on the tool (measured at 120 mm from the front side of the bearing) versus radial displacement at different bearing supply absolute pressures

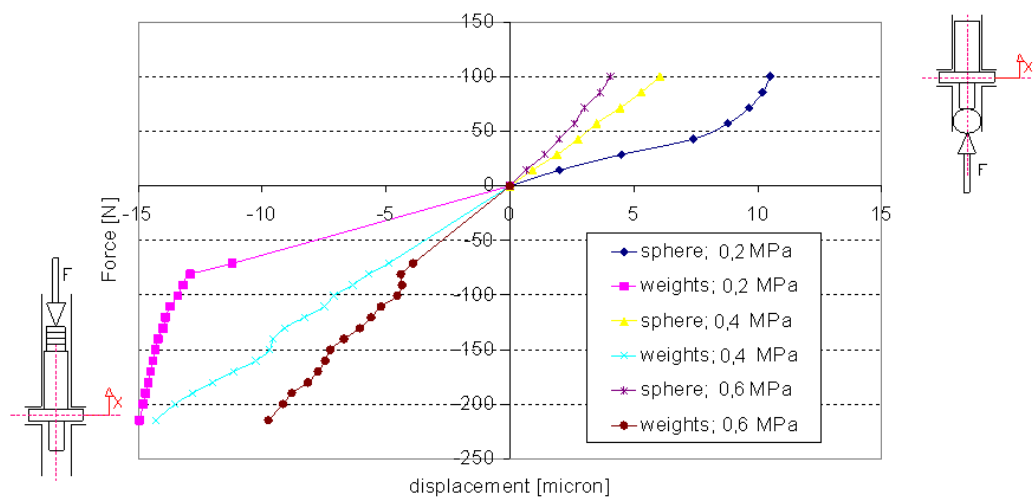


Figure 13. Diagram of axial force on tool versus displacement at different bearing supply gauge pressures

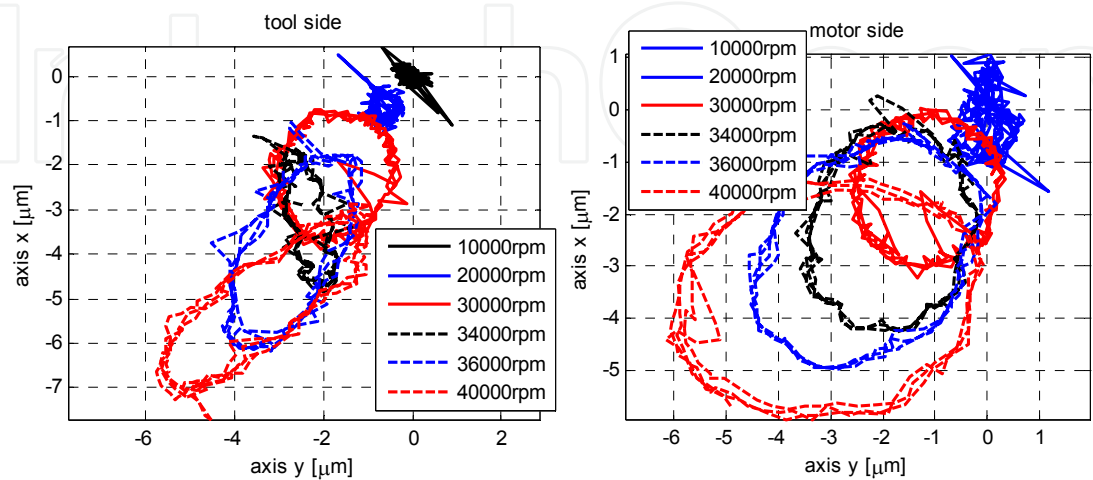


Figure 14. Rotor orbits in correspondence of a bushing due to the residual unbalance; supply gauge pressure 0.6 MPa

The electro-spindle was also tested in dynamic conditions during machining with high speed milling cutters of diameters in the range 1 to 6 mm. The system depicted in Figure 15, mounted below the electro-spindle, provides the advance along axis x of the material under milling. The material under machining was a block of rapid prototyping resin, advanced by means of a motorized slide. The tests were made up to 40000 rpm with feed speeds from 1 to 10 mm/s and chip thickness 1 mm.

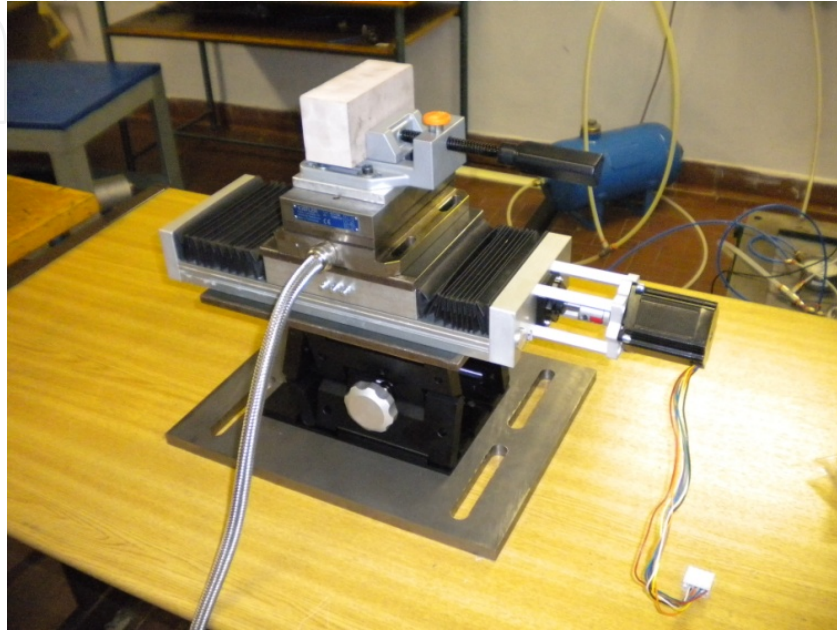


Figure 15. Motorized slide used for the dynamic tests

4. The textile rotor with damping supports

Gas bearings suffer from instability problems at high speed. A method to increase the stability threshold (the speed at which the unstable whirl occurs) is to increase the damping of the rotor-bearings system by introducing external damping supports [16]. A design guideline for the selection of the support parameters that insure stability in an aerodynamic journal bearing with damped and flexible support is given in paper [2].

The prototype described in this paragraph was designed with the priority of increasing the stability at high speeds [17]. The method adopted for this purpose was the use of rubber O-rings.

The prototype consists on a rotor (1) made of hardened 32CrMo4 steel with mass 0.96 kg, diameter 37 mm and length 160 mm. The rotor is supported by a radial air bearing mounted on rubber O-rings and an axial thrust bearing (Figure 16). It was designed to rotate in stable conditions up to 150 krpm. At one end of the rotor an air turbine (2) was machined and at the other end a nose (3) was screwed to the rotor. The housing (4) is fixed to the base and has four circumferential slots in which the O-rings are inserted. The bushing (5) incorporates the rubber rings and has four sets of supply nozzles (diameter 0.2 ± 0.01 mm) fabricated by EDM. The total length of the bearings is 57 mm. In the middle plane of the bushing a

discharge slot (6) is vented by a radial hole in the housing (see Figure 17). A central annular discharge chamber separates the radial bearings.

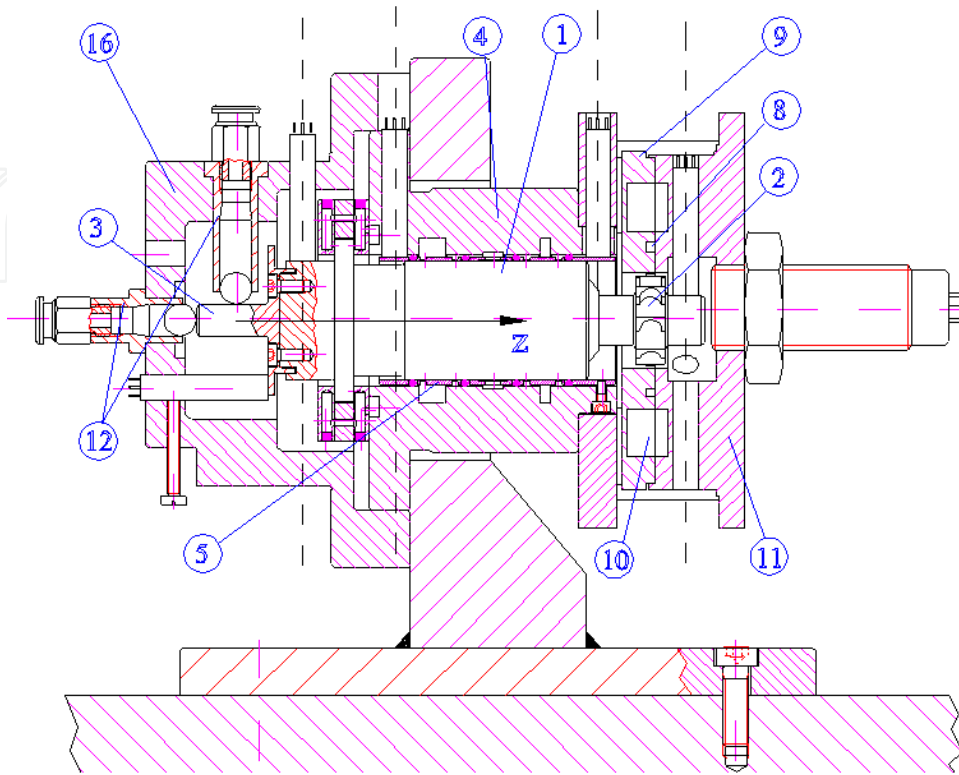


Figure 16. Test bench of the floating bushing

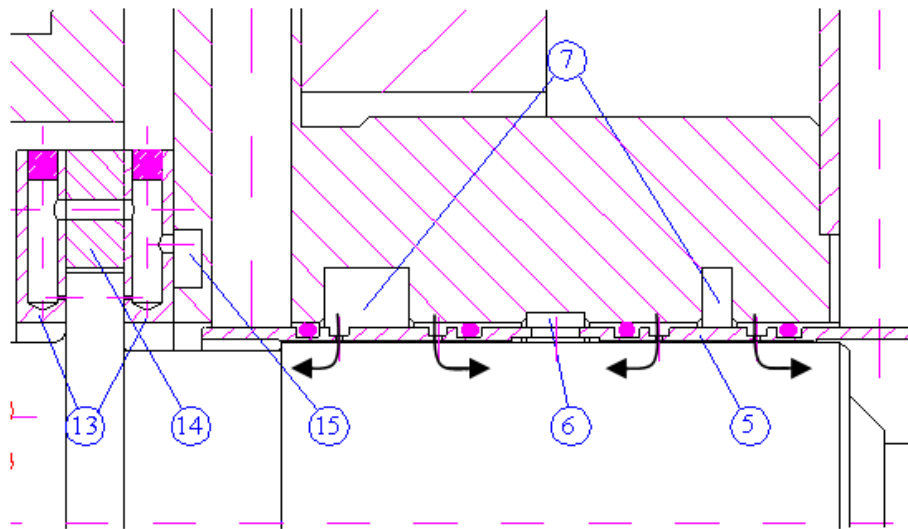


Figure 17. Enlargement of the floating bushing

The air from supply slots (7) flows to the radial clearance through the nozzles to reach the vent centrally in the discharge slot and laterally. The purpose of the O-rings, besides providing a seal between supply slots and discharge chamber, is to introduce damping in the rotor-bearing system. The turbine is driven by tangential jets discharged through 8

nozzles (8) machined on distributor (9). Annular chamber (10) connected to the nozzles is supplied through an axial hole on pre-distributor (11). Air is exhausted after actuating the turbine. Open loop speed control is maintained by setting the turbine supply pressure. The rotational speed was measured by an optical tachometer consisting of an emitter and a receiver facing the rotor at the turbine side. A retro-reflector stuck to a portion of the rotor face reflects emitted signal once per revolution.

Radial and axial forces are applied to the nose by means of loading systems (12) similar to the ones previously described. Eight capacitive displacement transducers are inserted radially in the housing, the pre-distributor and cover (16) to sense the rotor and bushing positions. An axial transducer can be inserted near the nose to monitor the axial position of the rotor with respect to the thrust bearing.

The O-Rings have 41 mm inside diameter and 70 Shore hardness. The three materials used for testing are NBR (Butadiene Acrylonitrile), Viton® (Fluorinated Hydrocarbon) and Silicone (Polysiloxane).

Accurate dimensional checks were carried out to evaluate axial and radial clearances, supply holes diameter and O-ring interference. The total diametral gap between them was found to be $35 \pm 2 \mu\text{m}$. The difference between the thickness of central ring (14) and rotor flange was $19 \pm 2 \mu\text{m}$, giving an axial clearance of approximately $9.5 \mu\text{m}$.

To measure the diameter of the nozzles supplying the bearings an optical fibre camera with 200X magnifying lens was used. The measurements were accurate and repeatable, thus proving the superiority of EDM technology over micro-drilling. Figure 18 shows a sample photographic record at 200X magnification.

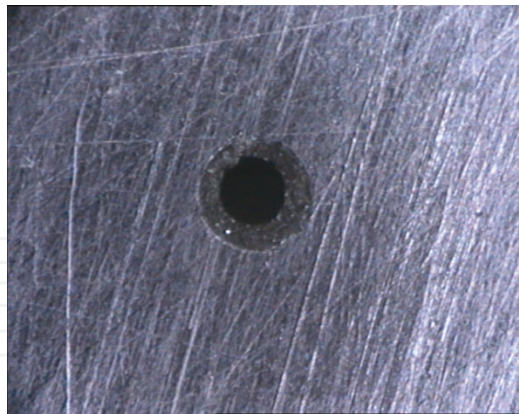


Figure 18. Supply hole magnification (200X)

The supply hole diameter, after fixing the radial clearance, is selected on the basis of numerical investigation conducted to simulate the dynamic behaviour of the system. The mathematical model used for this purpose is described in a separate paragraph at the end of this chapter.

O-ring grooves in the housing have a medium diameter of 43.5 mm, while external diameter of the bushing is 41 mm. The cross section diameter d of the rings was determined by a shadow comparator.

Table 3 lists the interferences on the O-rings calculated using the equation

$$int\% = \left(d - \frac{D_i - D_e}{2} \right) \frac{100}{d}$$

where D_i and D_e are the inside diameter of the grooves machined in the housing and the external diameter of the bushing respectively. With 0.6 MPa pressure differential the sealing function of the rubber rings between chambers 7 and 6 was realized with interference about 10% or more.

In Table 4 the measures of the inner diameter d and the cross-section diameter d_c are shown.

	Cross section diameter d [mm]	Interference
NBR-Silicone	1.78±0.01	30%
Viton	1.73±0.01	28%

Table 3. Interference values

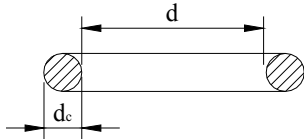
		
	d (mm)	d_c (mm)
NBR	41	1.80
Viton	41	1.83
Silicone	41	1.83

Table 4. Dimensions of the O-rings

4.1. Measured rubber dynamic stiffness

The dynamic stiffness of rubber O-rings is measured in order to introduce into the model the stiffness and the viscous equivalent damping. These parameters depend on the vibration frequency and also on the radial displacement imposed. Tests were made under different conditions, varying the diametral interference on the O-ring and the displacement amplitude x_0 imposed, in the frequency range 300÷800 Hz. In Figure 19 is visible the scheme of the test rig, in which the cylinder is fixed and the casing is mounted on the shaker plate. The force amplitude F_0 is measured by the load cell mounted between two fixed parts.

Measurements were made at different radial amplitudes. Increasing x_0 both stiffness and damping decrease. The results visible in Figure 20 were obtained with $x_0=25 \mu\text{m}$ and a diametral interference of 11%, that are similar to that occur in the air bearing test bench. The results obtained with Silicone are not reported because the FRF of transfer function F/x was very noisy.

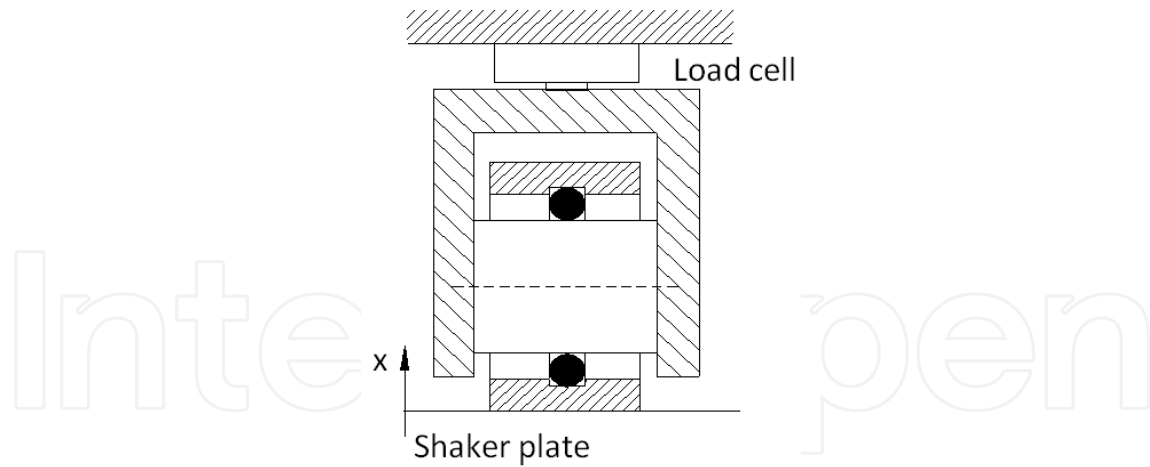


Figure 19. Scheme of the O-ring test rig

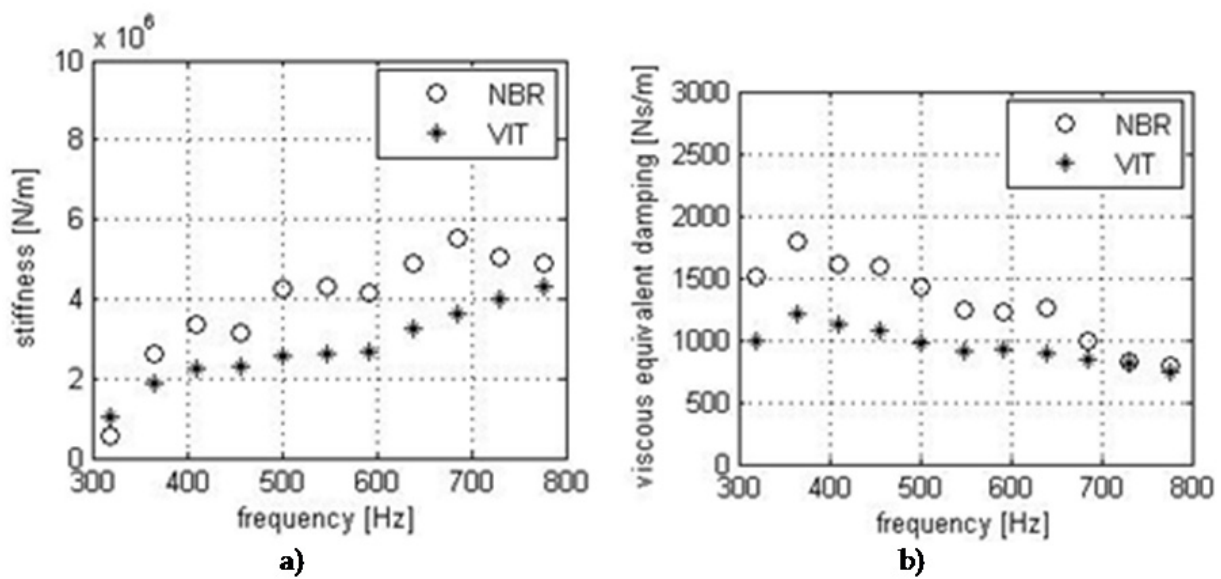


Figure 20. O-ring radial stiffness (a) and damping (b)

4.2. Stability

The response to a rotor radial step jump displacement of $1 \mu\text{m}$ from coaxial position is calculated. As a first approximation, average values of O-ring stiffness k_{OR} and damping c_{OR} are considered, neglecting the dependence on the frequency.

The parameters introduced in the model are shown in Table 5. L_1 and L_2 are the axial lengths of the two radial bearings.

$m_{\text{rot}}=0,97 \text{ kg}$	$h_0=17 \mu\text{m}$	$L_2=23 \text{ mm}$	$T^0=293 \text{ K}$
$m_b=0,1 \text{ kg}$	$d_s=0,2 \text{ mm}$	$\mu=1,81\text{e-}5 \text{ Ns/m}^2$	$k_{\text{OR}}=4 \cdot 10^6 \text{ N/m}$
$R=18.5 \text{ mm}$	$L_1=25 \text{ mm}$	$R^0=287 \text{ J/kgK}$	$c_{\text{OR}}=1 \cdot 10^3 \text{ Ns/m}$

Table 5. Input values of the model

In Figure 21 the theoretical supply pressure values in correspondence to the stability threshold are plotted vs. the rotational speed for the cases of fixed bearing and bearing mounted on O-rings. Each curve divides the plane into two regions: the upper one relative to a stable behaviour of the rotor-bearing system, the lower one relative to an unstable behaviour. In the first case, as a result of an initial step jump displacement of the rotor, the system evolves to the centred position (punctual stability); in the second case the rotor trajectory is an open spiral and causes the contact between the rotor and the bushing. In correspondence to the threshold curves the system evolves to a condition of orbital stability. The stabilizing effect of the rubber rings is evident because the pressure that guarantees the stability is lower.

In Figure 22 the simulated values are compared with the experimental ones, relative to three kinds of rubber: NBR, Viton and Silicone. There is good agreement between the experimental and the simulated stability threshold also if the experimental data are influenced by the rotor imbalance and in calculations the effect of imbalance is neglected (the rotor was dynamically balanced to a grade better than ISO quality grade G-2.5).

The whirling frequency ω increases with the rotational speed, see Figure 23. It is interesting to observe that the whirling ratio $\gamma = \omega/\Omega$ at the stability threshold (Figure 24) decreases with the rotational speed.

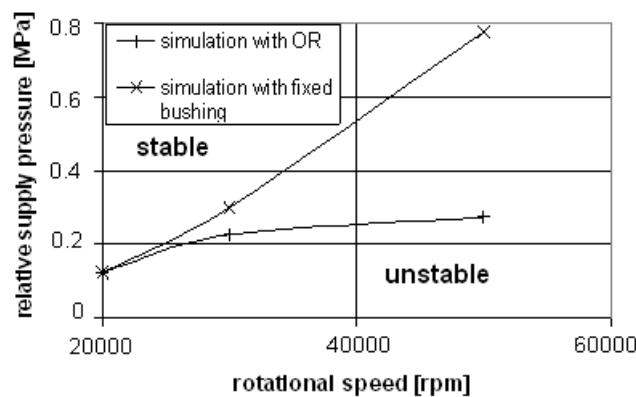


Figure 21. Theoretical results with fixed bearing and bearing mounted on OR

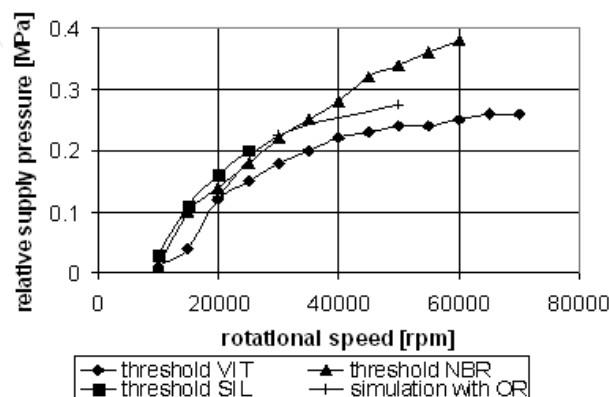


Figure 22. Comparison between experimental and simulated threshold stability

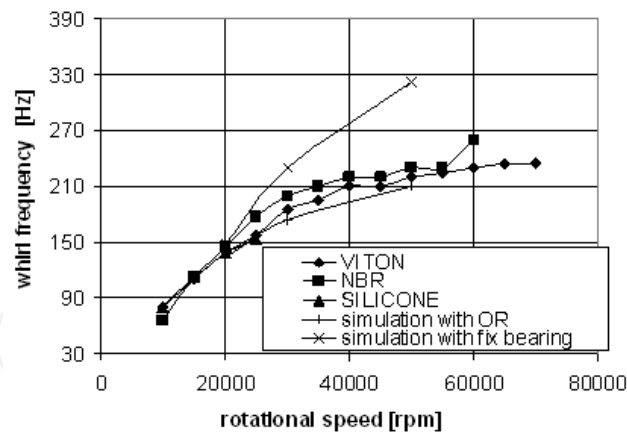


Figure 23. Comparison between experimental and simulated whirling frequency ν

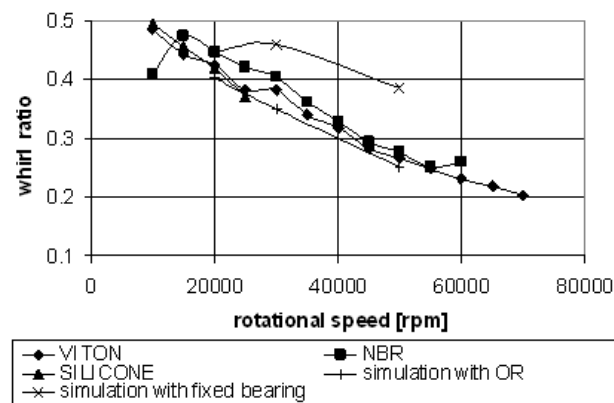


Figure 24. Comparison between experimental and simulated whirling ratio γ

It is possible to approach this threshold by decreasing the supply pressure or by increasing the rotational speed. Both possibilities are treated: Figures 25 and 26 show the change of the orbit amplitude vs these parameters. The increase in amplitude near stability threshold is sudden and considerable in both cases.

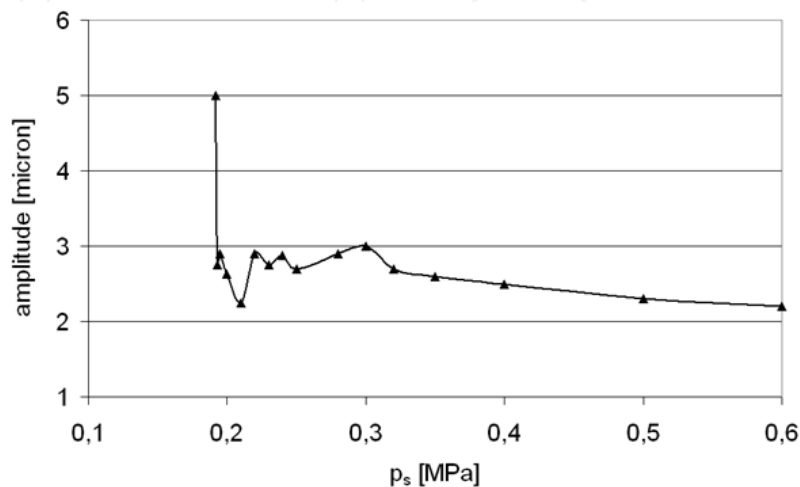


Figure 25. Orbit amplitude versus supply pressure; $\omega=30000$ rpm

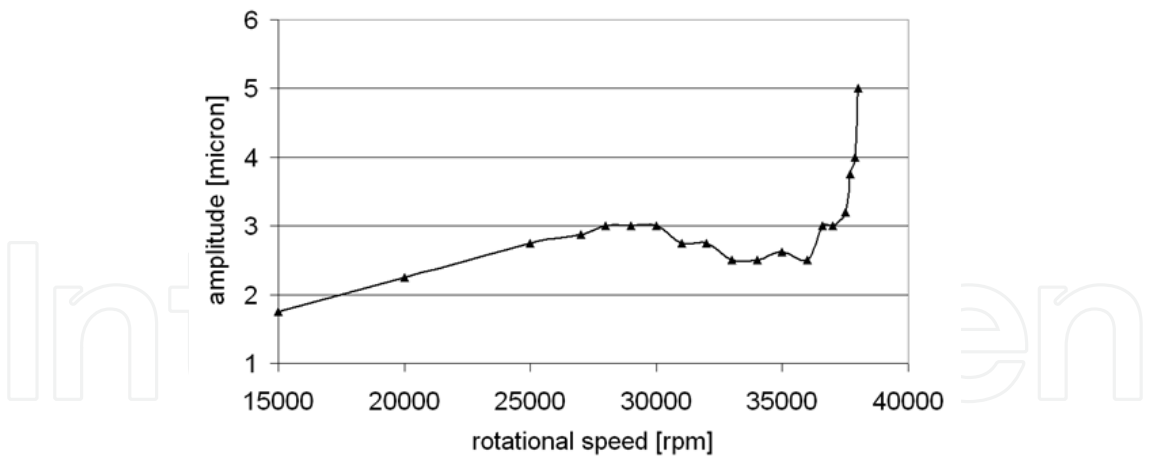


Figure 26. Orbit amplitude versus rotational speed; $p_s=0.22$ Mpa

Figure 27 shows the change in orbit shape with decreasing the supply pressure. Whirl motion is conical for any supply pressure at the stability threshold. Frequency spectra for turbine displacement in the two conditions are visible in Figure 28.

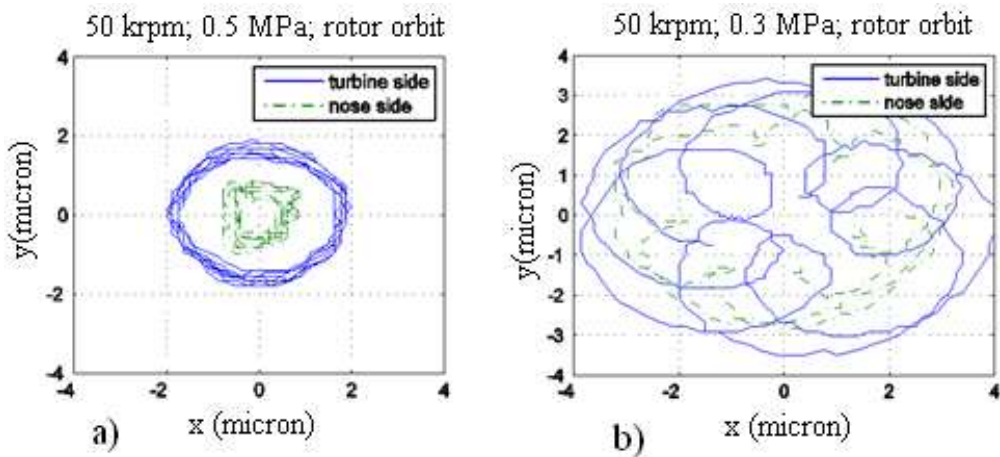


Figure 27. Rotor orbits in stable condition (a) and at stability threshold (b); $\omega=50000$ rpm

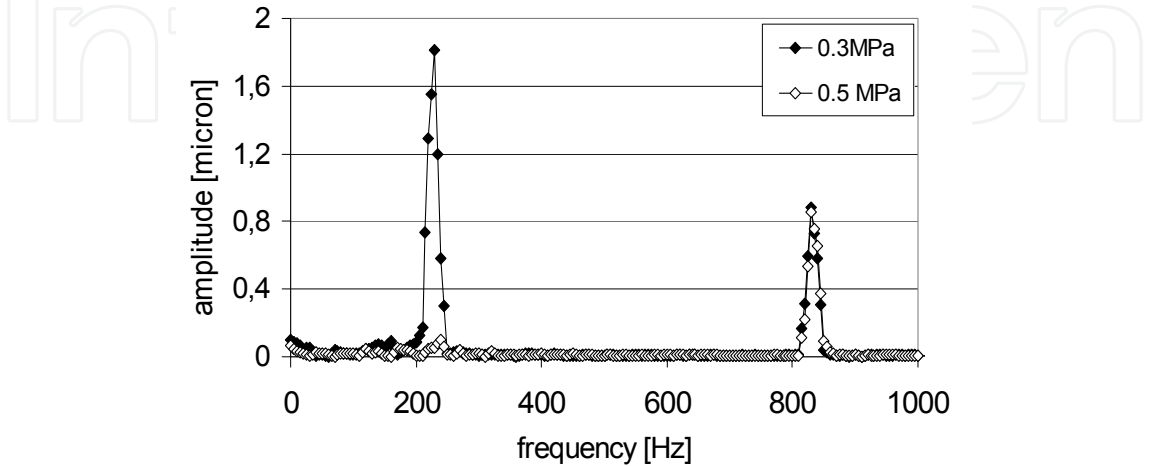


Figure 28. Frequency spectra of rotor displacement; $\omega=50$ krpm

5. The mesoscopic spindle

Another method to increase the bearing stability is to modify the film geometry from the circular journal bearing profile. Non-circular journal bearings can assume various geometries: elliptical [20-23] offset halves [24] and three-lobe configuration [25,26] are the most common geometries. Paper [27] shows a comparative analysis of three types of hydrodynamic journal bearing configurations namely, circular, axial groove, and offset-halves.

There is an extensive literature about the study of the dynamic stability of hydrodynamic journal bearings with non-circular profile, but very few papers consider gas journal bearings of this type. The wave bearing with compressible lubricants was introduced in the early 1990's [28,29].

In the present paragraph the design of the elliptical and multi-lobes gas bearings for a ultra-high speed spindle is described [30].

The bearings were designed to have a stable regime of rotation up to 500 krpm with acceptable stiffness and load characteristics. A computerized design was used for optimization of the rotor-bearing characteristics. The bearing clearance was represented by expression

$$h = h_0 \left(1 + \frac{c_{form}}{2} (\cos(n\vartheta) - 1) \right)$$

where c_{form} is the profile form factor, h_0 is the maximum clearance and n is the number of lobes of the profile.

The static and dynamic performances were numerically analyzed for two pairs of radial externally pressurized gas bearings. Conical and cylindrical whirl modes were considered. From numerical simulations for a 10 mm diameter rotor, bearing clearances non less than 5 μm and supply pressure 0.6 MPa the following results were obtained:

- the maximum rotor speed obtained with circular bearing (clearance 5 μm) with 4 supply orifices of 0.1 mm diameter in circumferential direction was 150 krpm, while with 32 supply orifices of 0.2 mm diameter was 250 krpm;
- with elliptical bearing profile the maximum rotor speed obtained with stable operation was 500 krpm for bearings with 4 supply orifices of 0.2 mm diameter in circumferential direction;
- the rotor with the multi-lobe bearings were less stable in comparison with the rotor with elliptical bearings;
- the positioning of supply orifices at 45° with respect to the principal axes of the elliptic profile improved bearing characteristics.

The final bearing geometry is defined by the parameters summarized in Table 6. Each elliptical journal bearing presents two rows of 4 supply orifices positioned at 45° with respect to the principal axes.

Maximum clearance h_0 , μm	15
Rotor diameter, mm	10
Supply orifice diameter, mm	0.2
Number of supply orifices for each bearing	8
Number of bearings	4
Profile form factor C_{form}	0.7
Number of profile lobes n	2

Table 6. Final bearing parameters

Figure 29 shows the prototype of ultra-high speed spindle. The rotor, of mass 0.07 kg, is supported by two pairs radial elliptical bearings and a double thrust bearing. The calculated radial stiffness on the rotor end is 3 N/ μm and the air consumption is $3.65 \cdot 10^{-4}$ kg/s.

The axial and the radial stiffness of the bearings were measured with test benches realized at the purpose (Figure 30). The axial and radial displacement of the rotor due to an imposed load was measured by laser beams. The axial stiffness of the thrust supplied at 0.6 MPa is 2.8 N/ μm , while the radial stiffness is 1 N/ μm . This value can be increased with a better dimensional control of the bearings internal profile.

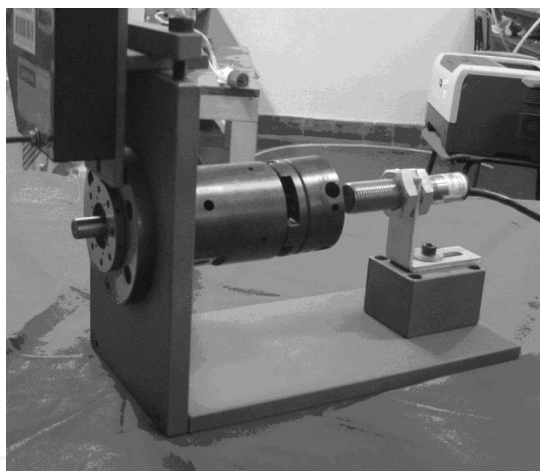


Figure 29. Ultra-high speed spindle prototype

By means of start-up (acceleration) and coast down (deceleration) tests on the spindle the bearing friction torque was estimated as a function of the speed up to 150000 rpm. The deceleration tests from different rotational speeds are depicted in Figure 31. The friction torque was found to be proportional to the rotational speed with the rate of 10^{-4} Nm every 10000 rpm. The dynamic runout of the shaft was measured by means of laser beams at different rotational speeds in correspondence of the nose.

The unbalance response was synchronous and unstable whirl was not encountered. In Figure 32 the waterfall diagram, obtained with the FFT of the shaft radial vibration, is shown. There is a critical speed at 34000 rpm, to which corresponds a maximum spindle runout of $\pm 9 \mu\text{m}$.

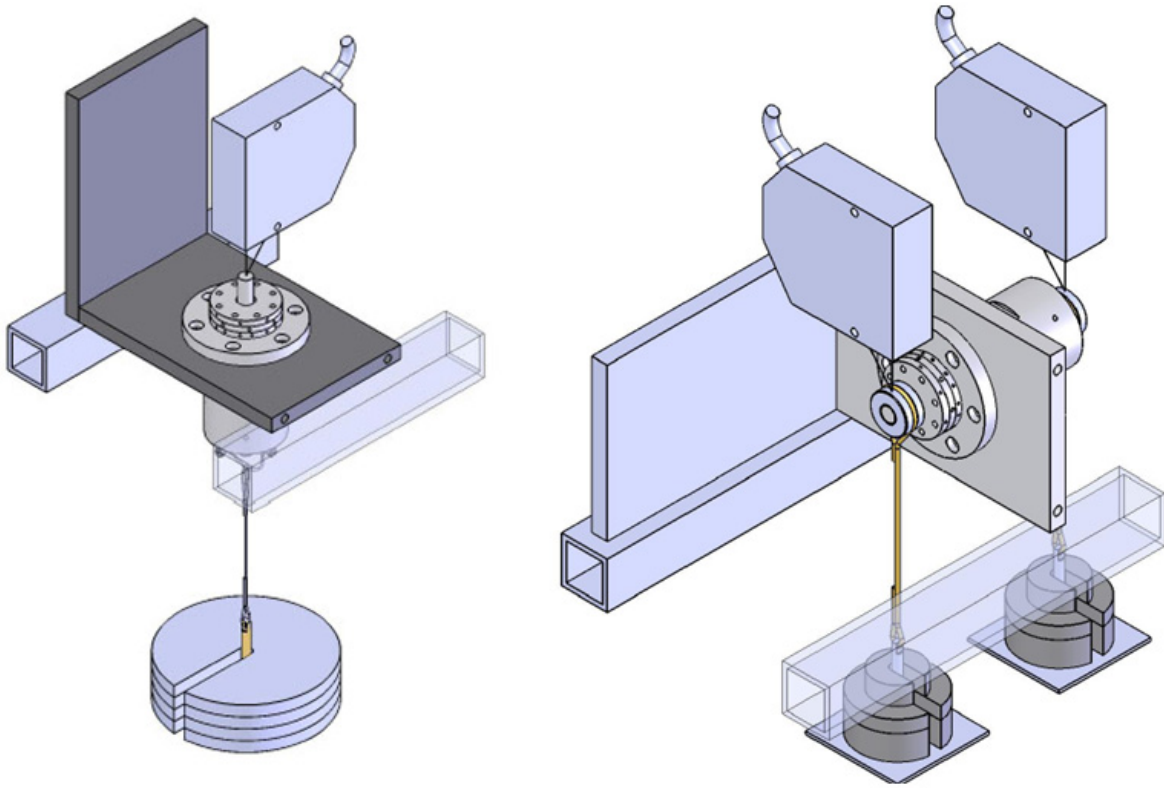


Figure 30. Test benches realized to measure the radial and axial bearing stiffness

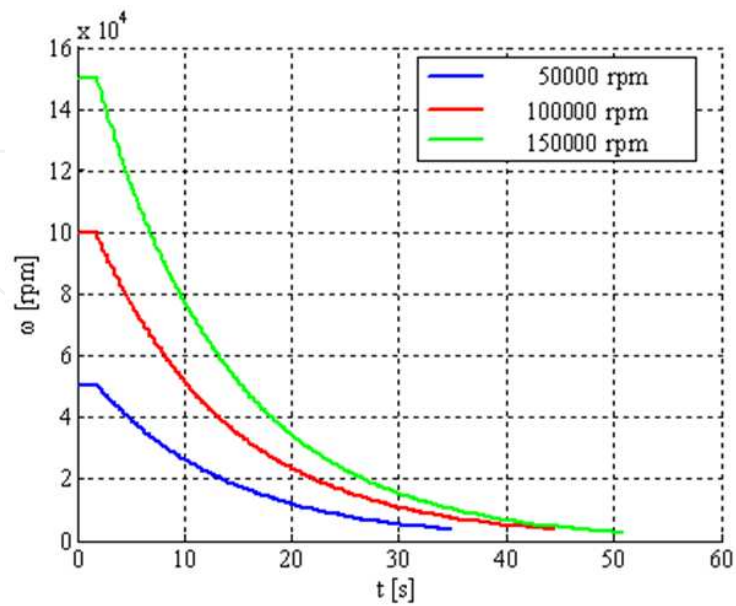


Figure 31. Test benches realized to measure the radial and axial bearing stiffness; supply gauge pressure 0.6 MPa

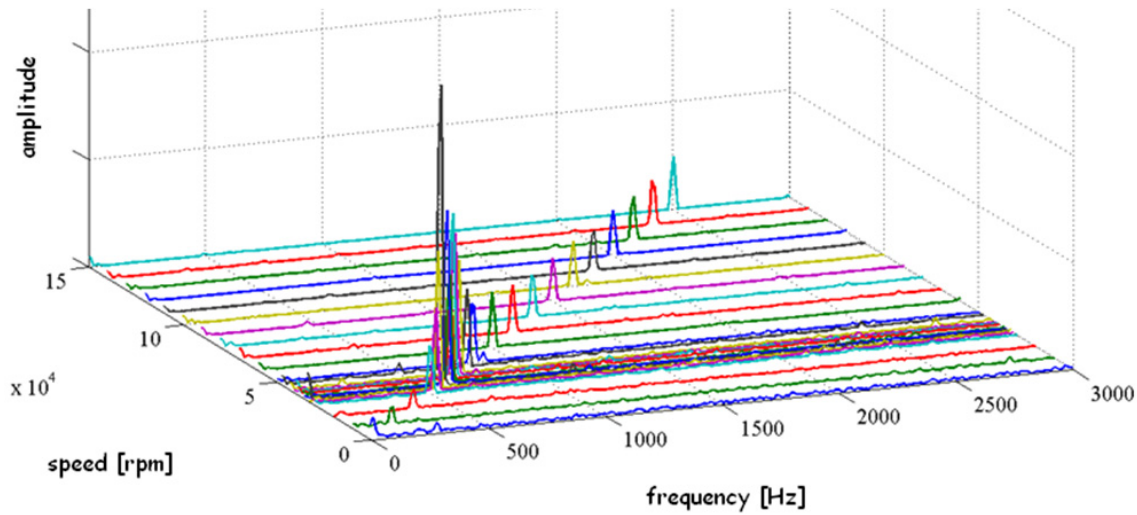


Figure 32. Waterfall diagram of the rotor unbalance response

6. Mathematical model

The complete Reynolds equation for compressible fluid film is numerically solved together with the equations of motion of the rotor considered rigid, see reference [18].

The momentum equations for the isothermal gas lubricated films are:

$$\frac{p}{R^0 T^0} \left(\frac{\partial u}{\partial t} + u \frac{\partial u}{\partial z} + v \frac{\partial u}{R \partial \vartheta} \right) + \frac{\partial p}{\partial z} = -\mu \frac{12u}{h^2} \quad (1)$$

$$\frac{p}{R^0 T^0} \left(\frac{\partial v}{\partial t} + u \frac{\partial v}{\partial z} + v \frac{\partial v}{R \partial \vartheta} \right) + \frac{\partial p}{R \partial \vartheta} = \mu \frac{6(R\omega - 2v)}{h^2} \quad (2)$$

where u and v are the mean velocity components in z - and θ -direction (Figure 33).

They are solved together with the continuity equation

$$\frac{\partial(ph u)}{\partial z} + \frac{\partial(ph v)}{R \partial \vartheta} + \frac{\partial(ph)}{\partial t} - R^0 T^0 q = 0 \quad (3)$$

where q is the inlet mass flow rate per unit surface defined by

$$q = \frac{G}{\Delta z R \Delta \vartheta} \quad (4)$$

For low modified Reynolds numbers ($Re^* = \rho \omega h_0^2 / \mu < 1$) inertial terms are negligible. The equation resulting from (1-3) is simplified into the following

$$\frac{\partial}{\partial z} \left(p h^3 \frac{\partial p}{\partial z} \right) + \frac{\partial}{R \partial \vartheta} \left(p h^3 \frac{\partial p}{R \partial \vartheta} \right) + 12 \mu R^0 T^0 q = 6 \mu \omega \frac{\partial(ph)}{\partial \vartheta} + 12 \mu \frac{\partial(ph)}{\partial t} \quad (5)$$

Film thickness h is given by

$$h(\vartheta, z) = h_0 - e_x(z) \cos \vartheta - e_y(z) \sin \vartheta \quad (6)$$

The rotor eccentricities e_x and e_y are related to the journal degrees of freedom by

$$e_x(z) = x_G + (z - z_G)\vartheta_y; e_y(z) = y_G - (z - z_G)\vartheta_x \quad (7)$$

Concerning the thrust bearing, the Reynolds equation is

$$r^2 \frac{\partial}{\partial r} \left(p h^3 \frac{\partial p}{\partial r} \right) + \frac{\partial}{\partial \vartheta} \left(p h^3 \frac{\partial p}{\partial \vartheta} \right) + 12 \mu R^0 T^0 r^2 q = 6 \mu \omega r^2 \frac{\partial (p h)}{\partial \vartheta} + 12 \mu r^2 \frac{\partial (p h)}{\partial t} \quad (8)$$

The boundary conditions at the discharge slots are $p=p_a$, while in correspondence of the supply ports the downstream pressure level is calculated considering orifice resistance.

The input resistance is expressed on the basis of ISO formula for flow rate through an orifice (ISO, 1989).

$$G = \begin{cases} c_s k_T \rho_N p_s & \text{if } 0 < \frac{p}{p_s} < b \\ c_s k_T \rho_N p_s \sqrt{1 - \left(\frac{\frac{p}{p_s} - b}{1-b} \right)^2} & \text{if } b < \frac{p}{p_s} < 1 \\ -c_s k_T \rho_N p \sqrt{1 - \left(\frac{\frac{p}{p_s} - b}{1-b} \right)^2} & \text{if } 1 < \frac{p}{p_s} < \frac{1}{b} \\ -c_s k_T \rho_N p & \text{if } \frac{p}{p_s} > \frac{1}{b} \end{cases} \quad (9)$$

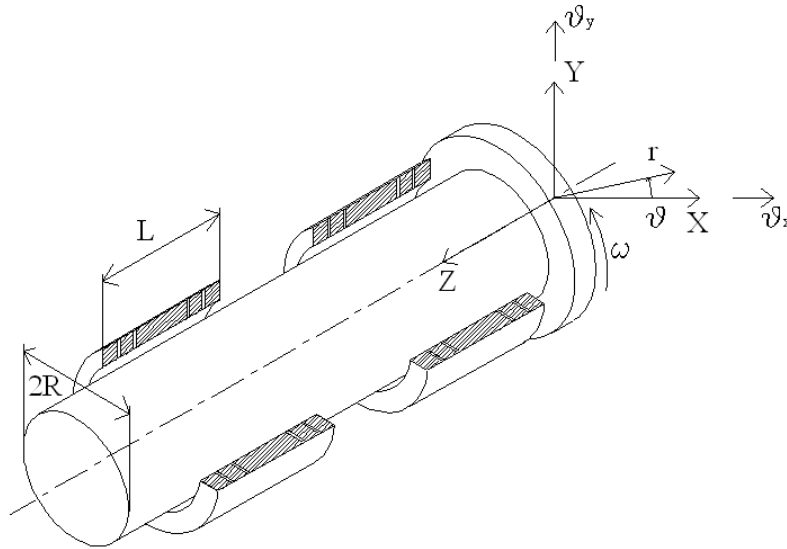


Figure 33. Schematic diagram of journal bearings

Conductance c_s appearing in the mass flow rate formula is expressed by equation (10),

$$c_s = 0.686 \frac{c_d S}{\rho_N \sqrt{R^0 T^0}} \quad (10)$$

where c_d is the discharge coefficient and S the cross-section of the supply orifice.

Discharge coefficient c_d depends on local clearance h , supply port diameter d_s and Reynolds number Re of supply port section. This relationship is taken into account with equation (11), see ref. [19].

$$c_d = 0.85 \left(1 - e^{-8.2 \frac{h}{d_s}} \right) (1 - e^{-0.005 Re}) \quad (11)$$

The Reynolds number is calculated with eq. (12)

$$Re = \frac{4G}{\pi d_s \mu} \quad (12)$$

Equation (11) is extrapolated from experimental measurements of air consumption and pressure distributions under pads for different air gap height and supply port sizes. The equation is extrapolated in the range of h/d_s values from $12.5 \cdot 10^{-3}$ to $100 \cdot 10^{-3}$.

The Reynolds equation is discretized spatially by central finite-differences:

$$3h_{i,j}^2 \left(\frac{\partial h}{\partial z} \right)_{i,j} \frac{p_{i+1,j}^2 - p_{i-1,j}^2}{2\Delta z} + h_{i,j}^3 \frac{p_{i+1,j}^2 - 2p_{i,j}^2 + p_{i-1,j}^2}{(\Delta z)^2} + 3h_{i,j}^2 \left(\frac{\partial h}{R\partial \vartheta} \right)_{i,j} \frac{p_{i,j+1}^2 - p_{i,j-1}^2}{2R\Delta \vartheta} + h_{i,j}^3 \frac{p_{i,j+1}^2 - 2p_{i,j}^2 + p_{i,j-1}^2}{(R\Delta \vartheta)^2} + 24R^0 T^0 \mu q_{i,j} = 12\mu\omega h_{i,j} \frac{p_{i,j+1} - p_{i,j-1}}{2\Delta \vartheta} + 12\mu\omega p_{i,j} \left(\frac{\partial h}{\partial \vartheta} \right)_{i,j} + 24\mu h_{i,j}^n \frac{p_{i,j}^{n+1} - p_{i,j}^n}{\Delta t} + 24\mu p_{i,j}^n \frac{h_{i,j}^{n+1} - h_{i,j}^n}{\Delta t} \quad (13)$$

The journal equations of motion are considered together with the Reynolds equation in order to study the dynamics of the rotor-bearings system.

The 4 d.o.f. model of the rotor is described by the following system

$$\begin{cases} m_r \ddot{x}_G = F_{cx} + F_x + m_r \varepsilon \omega^2 \cos(\omega t) \\ m_r \ddot{y}_G = F_{cy} + F_y + m_r \varepsilon \omega^2 \sin(\omega t) \\ J_G \ddot{\vartheta}_x = M_{cx} + F_y (z_G - z_F) - J_P \omega \dot{\vartheta}_y + \chi (J_P - J_G) \omega^2 \cos(\omega t - \varphi) \\ J_G \ddot{\vartheta}_y = M_{cy} - F_x (z_G - z_F) + J_P \omega \dot{\vartheta}_x + \chi (J_P - J_G) \omega^2 \sin(\omega t - \varphi) \end{cases} \quad (14)$$

where J_G is the rotor transverse inertia moment, calculated with respect to the rotor centre of mass, while J_P is the polar inertia moment. The external forces have a resultant of radial components F_x, F_y applied in correspondence of $z=z_F$.

The fluid forces, comprehensive of pressure and shear actions, are expressed by

$$\begin{cases} F_{cx} = \int_0^L \int_0^{2\pi} (p \cos \vartheta - \tau_\vartheta \sin \vartheta) R d\vartheta dz \\ F_{cy} = \int_0^L \int_0^{2\pi} (p \sin \vartheta + \tau_\vartheta \cos \vartheta) R d\vartheta dz \\ M_{cx} = \int_0^L \int_0^{2\pi} (-p \sin \vartheta + \tau_\vartheta \cos \vartheta) (z_G - z) R d\vartheta dz \\ M_{cy} = \int_0^L \int_0^{2\pi} (p \cos \vartheta + \tau_\vartheta \sin \vartheta) (z_G - z) R d\vartheta dz \end{cases} \quad (15)$$

The tangential actions are given by:

$$\tau_\vartheta = -\frac{h}{2} \frac{\partial p}{R \partial \vartheta} - \frac{\mu \omega R}{h} \quad (16)$$

The system is solved using Euler explicit method. From relation (17) the pressure for each node is calculated at iteration $n+1$.

$$p_{i,j}^{n+1} = p_{i,j}^n + \Delta t f \left(p_{i,j}^n, p_{i+1,j}^n, p_{i-1,j}^n, p_{i,j+1}^n, p_{i,j-1}^n, h_{i,j}^n, h_{i,j}^{n-1}, \left(\frac{\partial h}{\partial \vartheta} \right)_{i,j}^n, \left(\frac{\partial h}{\partial z} \right)_{i,j}^n \right) \quad (17)$$

The explicit method has a very rapid execution per time step but is limited to the use of small Δt , see [31]. The system of $n \times m$ equations (17) is solved together with rotor equations of motion (14).

The solution procedure starts with a set of input data (shaft diameter, radial clearance, bearing axial length, position and diameter of supply orifices, shaft speed).

To calculate the static pressure distribution, h is maintained constant in time and the system is solved with initial condition $p_{i,j}=p_a$ for each node. The rotor trajectory is determined starting with the initial static pressure distribution and using the following set of initial conditions:

$$x(0) = h_0 \varepsilon_x(0); y(0) = h_0 \varepsilon_y(0)$$

$$\dot{x}(0) = h_0 \dot{\varepsilon}_x(0); \dot{y}(0) = h_0 \dot{\varepsilon}_y(0)$$

The whirl stability can be verified with the orbit method [18,32], that considers the nonlinearities of the problem.

To analyze the dynamic properties of the thrust bearing the Reynolds equation (8) is solved in time together with the axial spindle equation of motion (18):

$$m_r \ddot{z} + F_t = F \quad (18)$$

in which F_t is the reaction force of the thrust bearing, F is the external axial force applied to the shaft and m_r is the rotor mass. The reaction force is calculated by integrating the pressure over the thrust surface.

7. Conclusions

This paper investigated four prototypes of high speed spindles and rotors supported by gas bearings. The radial and axial bearings were designed using a numerical program that simulates the pressure distribution inside the air clearance both in static and in dynamic conditions.

Different were the design priorities: stiffness and load capacity for the pneumatic spindle and the electro-spindle and stability for the textile spindle and the mesoscopic spindle. Two different methods were employed to increase stability: the introduction of external damping in the textile spindle and the modification of the film geometry in the mesoscopic spindle.

The experimental activity carried out demonstrated the suitability of gas bearings for different applications and made it possible to verify the numerical models. Experimental testing played an essential role in identifying the numerical models and in the same time the models, once identified, made it possible to save time in the design process. In particular the supply holes configuration of the prototypes was optimized using the numerical models to choose their number, diameter and disposition. For stability optimization of the mesoscopic spindle the models were used as virtual test benches to compare different geometries of bushing with non-circular profile. The results of the tests on rubber rings were used in numerical models to investigate their effect on stability.

The prototypes developed operated in stable conditions in the speed range expected. Future investigations will verify the stability at higher speeds.

8. Nomenclature

b	ratio of critical pressure to admission pressure, $b=0.528$
c_d	supply hole discharge coefficient
c_{OR}	damping coefficient of the O-ring
c_s	supply hole conductance
D	journal bearing diameter
d_s	supply hole diameter
F_t	external axial force on thrust bearing
F_x, F_y	external forces on rotor
G	air mass flow rate through the supply hole
h	local air clearance
h_0	clearance with rotor in centred position
J_G	transverse rotor moment of inertia, calculated respect to the centre of mass
J_P	polar moment of inertia of rotor
k_T	temperature coefficient, $k_T=\sqrt{293/T^0}$
k_{OR}	stiffness coefficient of the O-ring
L	bearing axial length
m_b	bushing mass
m_r	rotor mass
n, m	number of nodes along axial and circumferential directions
p	pressure
p_a	ambient pressure
p_s	bearing supply pressure
q	inlet mass flow rate per unit surface
R	journal bearing radius
r, θ, z	cylindrical coordinates
R^0	gas constant, in calculations $R^0=287.6 \text{ m}^2/\text{s}^2\text{K}$
Re	Reynolds number calculated at supply port section, $Re=4G/(\pi d_s \mu)$
Re^*	modified Reynolds number, $Re^*=q\omega h_0^2/\mu$
S	supply hole cross section
T^0	absolute temperature, in calculations $T^0=288 \text{ K}$
u, v	mean velocity components in z - and θ -direction
x, y, z	cartesian coordinates
z_G	center of mass axial coordinate
z_F	axial coordinate of the external force on the rotor
e_x, e_y	rotor eccentricities
Δt	time step
Δz	mesh size in axial direction
$\Delta \theta$	mesh size in circumferential direction
Λ	bearing number, $\Lambda=6\mu\omega/p_a(D/2h_0)^2$
χ	dynamic rotor unbalance

ε	static rotor unbalance
$\varepsilon_x, \varepsilon_y$	rotor eccentricity ratios
γ	whirl ratio, $\gamma=v/\omega$
φ	angle between static and dynamic unbalance
μ	dynamic viscosity, in calculations $\mu=17.89\cdot10^{-6}$ Pa·s
v	whirl frequency
ρ_N	air density in normal conditions
ω	rotor angular speed

Author details

G. Belforte, F. Colombo, T. Raparelli, A. Trivella and V. Viktorov

Department of Mechanical and Aerospace Engineering, Politecnico di Torino, Italy

9. References

- [1] Fuller, D.D. (1984), *Theory and practice of lubrication for engineers*, John Wiley and Sons, New York.
- [2] Waumans, T.; Peirs, J.; Al-Bender, F.; Reynaerts, D. (2011), Aerodynamic bearing with a flexible, damped support operating at 7.2 million DN, *J. Micromech. Microeng.* Vol. 21, 104014.
- [3] Boffey, D. A.; Desay D. M. (1980). An experimental investigation into the rubber-stabilization of an externally-pressurized air-lubricated thrust bearing, *ASME Trans. Journal of lubrication technology*, Vol. 102, pp. 65-70.
- [4] Czolczynski K. (1994), Stability of flexibly mounted self acting gas journal bearings, *Nonlinear Science, Part B, Chaos and nonlinear Mechanics*, No. 7, pp. 286-299.
- [5] Zhang, R.; Chang H. S. (1995). A new type of hydrostatic/hydrodynamic gas journal bearing and its optimization for maximum stability, *STLE Tribology Transactions*, Vol. 38, No. 3, pp. 589-594.
- [6] Yang, D-W; Chen, C-H; Kang, Y.; Hwang, R-M.; Shyr, S-S. (2009). Influence of orifices on stability of rotor-aerostatic bearing system, *Tribology International*, Vol. 42, pp. 1206-1219.
- [7] Westwind (2008a). Online available: [http://www.westwind-airbearings.com/specialist/wafer Grinding.html](http://www.westwind-airbearings.com/specialist/wafer%20Grinding.html)
- [8] Westwind (2008b). Online available: <http://www.westwind-airbearings.com/pcb/overview.html>
- [9] APT, Air Bearing Precision Technology. Catholic University of Leuven, Belgium. Online available: http://www.mech.kuleuven.be/industry/spin/APT/default_en.
- [10] Ohishi, S.; Matsuzaki, Y. (2002). Experimental investigation of air spindle unit thermal characteristics. *Precision Engineering*, Vol. 26, pp. 49-57.
- [11] Moore Precision Tools (2001). *Nanotechnology Systems*.
- [12] Precitech Precision, (2001). *Nanoform® 350 Technical Overview and Unsurpassed Part Cutting Results*.
- [13] Toshiba Machine Co. Ltd. (2002). *High Precision Aspheric Surface Grinder*.

- [14] Belforte, G.; Colombo, F.; Raparelli, T.; Trivella, A.; Viktorov, V. (2008a). High speed electrospindle running on air bearings: design and experimental verification, *Meccanica*, Vol. 43, pp. 591-600.
- [15] Belforte, G.; Colombo, F.; Raparelli, T.; Viktorov, V.; Trivella, A. (2006). An experimental study of high speed rotor supported by air bearings: test rig and first experimental results, *Tribology International*, Vol. 39, pp. 839-845.
- [16] Della Pietra, L.; Adiletta, G. (2002). The squeeze film damper over four decades of investigations: part 1. Characteristics and operating features, *Shock Vib. Dig.*, vol. 34, pp. 3-26.
- [17] Belforte, G.; Colombo, F.; Raparelli, T.; Trivella, A.; Viktorov, V. (2008b). High speed rotors with air bearings mounted on flexible supports: test bench and experimental results. *ASME Journal of Tribology*, Vol. 130, 1-7.
- [18] Belforte, G.; Raparelli, T.; Viktorov, V. (1999). Theoretical investigation of fluid inertia effects and stability of self-acting gas journal bearings. *ASME Journal of Tribology*, Vol. 121, 836-843.
- [19] Belforte, G.; Raparelli, T.; Viktorov, V.; Trivella, A. (2007). Discharge coefficients of orifice-type restrictor for aerostatic bearings, *Tribology International*, Vol. 40, pp. 512-521.
- [20] Mishra, P. C.; Pandley R. K.; Athre K. (2007). Temperature profile of an elliptic bore journal bearing, *Tribology International*, Vol. 40, pp. 453-458.
- [21] Hashimoto, H. (1992). Dynamic characteristic analysis of short elliptical journal bearings in turbulent inertial flow regime, *STLE Tribology Transactions*, Vol. 35, No. 4, pp. 619-626.
- [22] Hashimoto, H.; Matsumoto K. (2001). Improvement of operating characteristics of high speed hydrodynamic journal bearings by optimum design: Part I – formulation of methodology and its application to elliptical bearing design, *ASME Journal of Tribology*, Vol. 123, pp. 305-312.
- [23] Wang N. Z.; Ho C. L.; Cha K. C. (2000). Engineering optimum design of fluid film lubricated bearings, *Journal of Tribology Transactions*, Vol. 43, No. 3, pp. 377-386.
- [24] Read, L.J.; Flack, R.D. (1987). Temperature, pressure and film thickness measurements for an offset half bearing. *Wear*; Vol. 117, No. 2, pp. 197-210.
- [25] Ene, N. M; Dimofte, F. & Keith Jr., T. G. (2008a). A dynamic analysis of hydrodynamic wave journal bearings, *STLE Tribology Transactions*, Vol. 51, No. 1, pp. 82-91.
- [26] Ene, N. M; Dimofte, F. & Keith Jr., T. G. (2008b). A stability analysis for a hydrodynamic three-wave journal bearing, *Tribology International*, Vol. 41, No. 5, pp. 434-442.
- [27] Sehgal, R; Swamy, K.N.S.; Athre K.; Biswas S. (2000). A comparative study of the thermal behaviour of circular and non-circular journal bearings. *Lub Sci*, Vol. 12, No. 4, pp. 329-44.
- [28] Dimofte, F. (1995a). Wave journal bearing with compressible lubricant – Part I : The wave bearing concept and a comparison to the plain circular bearing, *Tribology Transactions*, Vol. 38, No. 1, pp. 153-160.
- [29] Dimofte, F. (1995b). Wave journal bearing with compressible lubricant – Part II : A comparison of the wave bearing with a groove bearing and a lobe bearing, *Tribology Transactions*, Vol. 38, No. 2, pp. 364-372.
- [30] Viktorov, V.; Belforte, G.; Raparelli, T.; Colombo, F. (2009). Design of non-circular gas bearings for ultra-high speed spindle. *World Tribology Congress*, Kyoto, 6-11 Sept. C1-212.
- [31] Castelli, V.; Pirviks, J. (1968) Review of numerical methods in gas bearing film analysis. *Journal of Lubrication Technology*, pp. 777-792.
- [32] Colombo, F.; Raparelli, T.; Viktorov, V. (2009). Externally pressurized gas bearings: a comparison between two supply holes configurations. *Tribology International*, Vol. 42, 303-310.